
LatticeVision: Image to Image Networks for Modeling Non-Stationary Spatial Data

**Antony Sikorski¹, Michael Ivanitskiy¹, Nathan Lenssen^{1,2}, Douglas Nychka¹,
Daniel McKenzie¹**

Colorado School of Mines¹

National Center for Atmospheric Research²

{asikorski, mivanits, lenssen, nychka, dmckenzie}@mines.edu

Abstract

In many scientific and industrial applications, we are given a handful of instances (a ‘small ensemble’) of a spatially distributed quantity (a ‘field’) but would like to acquire many more. For example, a large ensemble of global temperature sensitivity fields from a climate model can help farmers, insurers, and governments plan appropriately. When acquiring more data is prohibitively expensive—as is the case with climate models—statistical emulation offers an efficient alternative for simulating synthetic yet realistic fields. However, parameter inference using maximum likelihood estimation (MLE) is computationally prohibitive, especially for large, non-stationary fields. Thus, many recent works train neural networks to estimate parameters given spatial fields as input, sidestepping MLE completely. In this work we focus on a popular class of parametric, spatially autoregressive (SAR) models. We make a simple yet impactful observation; because the SAR parameters can be arranged on a regular grid, both inputs (spatial fields) and outputs (model parameters) can be viewed as images. Using this insight, we demonstrate that image-to-image (I2I) networks enable faster and more accurate parameter estimation for a class of non-stationary SAR models with unprecedented complexity.

1 Introduction

Modeling large, gridded spatial data has become a central challenge in many scientific and industrial applications. In situations where data is limited, parametric spatial processes can be fit to the existing data, enabling rapid simulation of additional fields. The bottleneck in this framework is inferring the statistical model parameters using maximum likelihood estimation (MLE), which becomes computationally intractable as dataset size increases [72, 75]. Moreover, spatial data over large domains frequently exhibit *non-stationarity*, meaning key parameters vary over space, further complicating parameter estimation. Many recent works have replaced MLE with neural networks, mapping spatial fields directly to local parameter estimates [39, 1, 87, 35]. Like MLE, these methods are limited to dividing large fields into smaller sections, each assumed to be stationary, and estimating parameters independently for each section. Although significantly faster than MLE, these local, neural estimation methods still scale linearly with the number of sections, and inherently struggle to capture long-range, global context.

In this work we introduce LatticeVision, a global estimation and emulation framework for large, non-stationary spatial data. We observe that for a popular group of statistical models known as spatial autoregressive (SAR) models, the parameters themselves are naturally arranged on a grid [47, 38]. *Thus, both the spatial fields of interest and their associated parameters can be viewed as images.*

Consequently, we adapt image-to-image (I2I) networks—both fully convolutional [59] and vision transformer based [16, 9]—to the task of estimating all model parameters at once. Our networks are

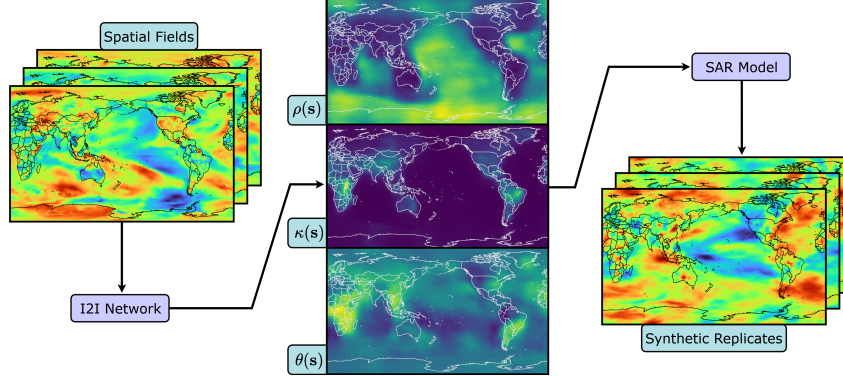


Figure 1: An illustration of the main workflow of LatticeVision. Spatial fields are fed into an I2I network, which in turn produces estimates of the non-stationary parameter fields. These are encoded into a SAR model from which synthetic replicates are efficiently simulated.

chosen to evaluate whether incorporating the attention mechanism [22, 5] improves performance over purely convolutional approaches [40], which have far fewer parameters. A key challenge in training these networks is ensuring they recognize complex non-stationarity patterns encountered in large, geoscientific data. Since we seek estimates for images (fields) of statistical parameters, the large, existing corpus of application-specific data [45, 26, 79] is not appropriate. Instead, we generate our own training data, encoding priors that represent the kind of non-stationary spatial processes expected for geophysical variables. After training, the networks can rapidly infer parameters from a limited number of observed fields, and use the well-known and computationally efficient LatticeKrig [47] SAR model to cheaply simulate as many synthetic fields as required.

As an illustrative example, we employ the LatticeVision framework on statistics derived from an Earth System Model (ESM). ESM simulations (‘runs’) model the long-term evolution of our climate, providing scientists, policymakers, agricultural planners, and other key stakeholders with critical projections that inform decision making and resilience planning. Additionally, many downstream analyses, such as those that estimate crop yield or flood risk, rely directly on the results of these runs as inputs [60, 77, 20]. The computational cost of performing more than a handful of ESM runs is extremely prohibitive, limiting ensemble sizes to 3-100 members [29, 57]; too few for robust uncertainty quantification of many climate impact models [66], quantifying internal ESM variability [43, 15], or capturing rare events [17]. Following parameter estimation, we generate realistic ensembles containing thousands of fields in a matter of seconds; a stark contrast to the tens of millions of core-hours required by ESMs.

In experiments with both simulated data and ESM outputs, I2I networks outperform local methods in accuracy—especially for detecting long-range, anisotropic correlations—as well as in computational efficiency. This advantage stems from their ability to estimate parameters for the entire spatial domain simultaneously, rather than by section [65] or by pixel [82]. Our approach also demonstrates improved robustness when inferring weakly-identifiable parameters from a small number of replicate spatial fields, which are represented as channels of the input image.

In summary, our work makes the following contributions:

- We propose a *global* framework for efficiently estimating non-stationary parameters with I2I networks, addressing the limitations of existing *local* approaches.
- We provide a strategy for generating training data that encodes scientifically meaningful priors that future estimators and emulators can use.
- We pair our novel, global estimators with a computationally efficient and flexible SAR model [47, 49] for rapid emulation, and validate this framework on ESM outputs.

All accompanying code for the experiments and results in this paper can be found at github.com/antonyxsik/LatticeVision.

2 Background: Gaussian Processes and SAR models

The past thirty years have seen the development of statistical models for spatial data that are invaluable for spatial prediction and emulation [24, 28, 18, 47, 14, 21]. Despite recent advances in generative networks [58, 62, 53, 36], statistical models remain useful when data is limited, and also contain interpretable parameters. These models are typically built around Gaussian processes (GPs). With locations $\mathbf{s} \in \mathbb{R}^2$, a mean-zero GP $f(\mathbf{s})$ is fully specified by its covariance function $k(\mathbf{s}, \mathbf{s}') = \mathbb{E}[f(\mathbf{s})f(\mathbf{s}')]$. The kernel k must be positive definite and this requirement is typically enforced by assuming *stationarity* and *isotropy* [13]. That is, k is independent of the location in the domain (stationarity), and depends only on the separation distance (isotropy):

$$k(\mathbf{s}, \mathbf{s}') = \sigma^2 \mathcal{C}(\kappa_m \|\mathbf{s} - \mathbf{s}'\|). \quad (1)$$

Here $\mathcal{C}(0) = 1$, σ^2 is the variance of the GP, and $\kappa_m > 0$ governs the spatial correlation range. A popular choice for \mathcal{C} is the Matérn family¹ with an additional parameter, $\nu > 0$, that controls the smoothness of process realizations. If $f(\mathbf{s})$ is a realization from the Matérn family with parameter ν , it will have $\lceil \nu \rceil - 1$ derivatives in a mean square sense. The Matérn class includes several common kernels as special cases (e.g., exponential and Gaussian), and its parameters have useful physical interpretations in geoscience. The primary obstacle to working with GP-based models is the computational cost ($\mathcal{O}(n^3)$ operations and $\mathcal{O}(n^2)$ memory for n spatial locations) of factorizing the covariance matrix $\Sigma \in \mathbb{R}^{n \times n}$ where $\Sigma_{ij} = k(\mathbf{s}_i, \mathbf{s}_j)$ [75].

The SPDE method. GPs from the Matérn family have an equivalent representation in terms of a stochastic partial differential equation (SPDE) [42, 81]:

$$(\kappa^2 - \Delta)^{(\nu+1)/2} f(\mathbf{s}) = \mathcal{W}(\mathbf{s}), \quad (2)$$

where κ^2 controls the correlation range, and is similar but not identical to κ_m in the Matérn, Δ is the Laplacian operator, and $\mathcal{W}(\mathbf{s})$ is a white noise Gaussian process with zero mean and variance σ^2 . The so-called (SPDE) method [38, 37] connects Matérn GPs to Gaussian Markov Random Fields (GMRFs) by demonstrating that discretizing Equation 2 on a regular grid yields a GMRF which approximates the Matérn GP well. This approach can be extended² to incorporate non-stationarity and anisotropy—a necessity for modeling complex geophysical processes such as the Earth’s climate—by incorporating a spatially varying dispersion matrix $H(\mathbf{s}) \in \mathbb{R}^{2 \times 2}$ and allowing κ^2 to vary in space:

$$(\kappa^2(\mathbf{s}) - \nabla \cdot H(\mathbf{s}) \nabla) f(\mathbf{s}) = \mathcal{W}(\mathbf{s}). \quad (3)$$

We construct $H(\mathbf{s})$ via its eigendecomposition³: $H(\mathbf{s}) = R(\mathbf{s})^\top D(\mathbf{s})^2 R(\mathbf{s})$ where

$$R(\mathbf{s}) = \begin{bmatrix} \cos(\theta(\mathbf{s})) & -\sin(\theta(\mathbf{s})) \\ \sin(\theta(\mathbf{s})) & \cos(\theta(\mathbf{s})) \end{bmatrix}, \quad D(\mathbf{s}) = \begin{bmatrix} \sqrt{\rho(\mathbf{s})} & 0 \\ 0 & 1/\sqrt{\rho(\mathbf{s})} \end{bmatrix} \quad (4)$$

The generalized Laplacian in Equation 3 can be written explicitly as

$$\nabla \cdot H(\mathbf{s}) \nabla \equiv H_{1,1}(\mathbf{s}) \frac{\partial^2}{\partial x^2} + 2H_{2,1}(\mathbf{s}) \frac{\partial^2}{\partial x \partial y} + H_{2,2}(\mathbf{s}) \frac{\partial^2}{\partial y^2}. \quad (5)$$

Interpreting the parameter fields. By specifying the “parameter fields” $\kappa^2(\mathbf{s})$, $\theta(\mathbf{s})$, and $\rho(\mathbf{s})$ we obtain a rich class of nonstationary GPs. Because we are defining this model in terms of (3), the problem of explicitly specifying an analytical form for the covariance that is positive definite is avoided. Moreover, these parameter fields are interpretable and can yield physical insights into the spatial dependence of the field. Specifically, κ^2 controls the overall range of correlation (larger κ^2 means more localized dependence), ρ controls the degree of anisotropy ($\rho = 1$ corresponds to isotropy), and θ controls the direction of anisotropy; see Figure 2.

¹In reviewing commonly used covariance kernels, [73] concludes: ‘Use the Matérn’ [38]

²For simplicity, we shall henceforth focus on the $\nu = 1$ case, the so-called Whittle covariance [81]

³This particular form of the eigendecomposition is for consistency with the literature [23]

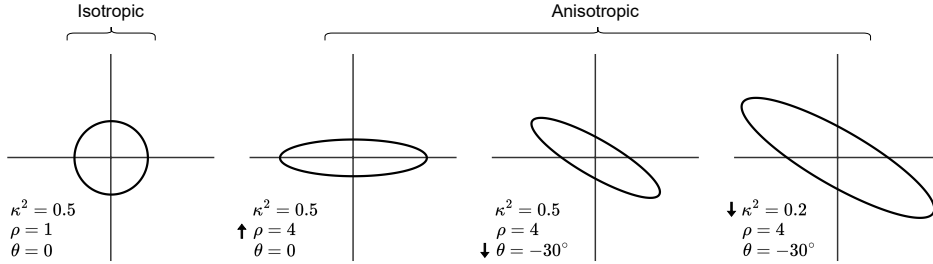


Figure 2: Illustration of the effects of κ^2 , ρ , and θ . The ellipses represent contours of constant correlation, e.g. all locations with correlation 0.5 with the origin. κ^2 controls the radii of the ellipse, ρ controls the ratio of the semi-major and semi-minor radii (i.e., the ‘aspect ratio’ of the ellipse), and θ is the angle the semi-major ellipse makes with the positive x -axis.

Discretizing the SPDE. To obtain a computable model from (3), one approximates this SPDE using either a finite element or finite difference method. Following [82]⁴ we use the finite difference method on a regular, evenly spaced grid, yielding the stencil:

$$\begin{array}{c|c|c} \frac{H_{1,2}(\mathbf{s})}{2} & -H_{2,2}(\mathbf{s}) & \frac{-H_{1,2}(\mathbf{s})}{2} \\ \hline -H_{1,1}(\mathbf{s}) & \kappa^2(\mathbf{s}) + 2H_{1,1}(\mathbf{s}) + 2H_{2,2}(\mathbf{s}) & -H_{1,1}(\mathbf{s}) \\ \hline \frac{-H_{1,2}(\mathbf{s})}{2} & -H_{2,2}(\mathbf{s}) & \frac{H_{1,2}(\mathbf{s})}{2} \end{array} \quad (6)$$

Let $\mathbf{y} \in \mathbb{R}^n$ denote a discretized solution to (3) on this grid, with $y_{i,j}$ denoting the value at grid location (i, j) . Then \mathbf{y} is the solution to $B\mathbf{y} = \mathbf{e}$ where $\mathbf{e} \sim \mathcal{N}(\mathbf{0}, I)$ is a sample from the standard multivariate normal distribution and $B \in \mathbb{R}^{n \times n}$ is the spatial autoregressive (SAR) matrix associated to the stencil (6). Lindgren et al [38] show that \mathbf{y} approximates a sample from the Matérn GP associated to (3). As B is sparse and structured (i.e., it is a banded matrix) this linear system may be solved at a computational cost $\mathcal{O}(n^{3/2})$, thus sidestepping the bottleneck associated with working with the GP directly. This formulation results in a GMRF with a particular SAR structure, where, by linear statistics, the precision matrix is computed as $Q = B^\top B$.

3 Non-stationary data generation

I2I data. In order for the I2I networks to be successful, the training data needs to encode priors appropriate for geoscientific applications. Previous work [82] has shown that coastlines, long-range East-West correlations due to jet streams, and oceanic circulation yield parameter fields that are important yet challenging to detect. So, we construct a pipeline for generating synthetic fields exhibiting these key phenomena. First, we construct spatially varying parameter fields $\kappa^2(\mathbf{s}), \rho(\mathbf{s}), \theta(\mathbf{s})$ and then use them to produce an M -replicate ensemble of synthetic fields $\mathbf{Y} = \{\mathbf{y}^{(m)}\}_{m=1}^M$, where each $\mathbf{y}^{(m)} \in \mathbb{R}^{H \times W}$. The parameter fields are concatenated along the channel dimension to form a three channel, ground truth “image” $\Phi \in \mathbb{R}^{3 \times H \times W}$, where $\Phi(\mathbf{s}) = [\kappa^2(\mathbf{s}), \rho(\mathbf{s}), \theta(\mathbf{s})]^T$. The replicates of the synthetic fields are also concatenated along the channel dimension to form the input image to our networks $\mathbf{Y} \in \mathbb{R}^{M \times H \times W}$. Thus, we have input-output pairs (\mathbf{Y}, Φ) in our data.

Each time we construct a single parameter field, we first sample one of eight spatial patterns $p^{(i)}(\mathbf{s}; \Omega^{(i)})$, $i = 1, 2, \dots, 8$. The patterns are simple spatial functions that dictate how a parameter will vary across the domain, and are designed to be caricatures of real geophysical variability. We hypothesize that these patterns will serve as “building blocks”, enabling our networks to generalize to the kinds of parameter changes that are present in geophysical settings. Each pattern is defined by its hyperparameters $\Omega^{(i)}$, which are randomly sampled from a series of prior uniform distributions. For example, when a “Coastline” pattern is selected, values that dictate the position and variation of the “Coastline” are chosen as well. The relative frequency and qualitative descriptions of these patterns are illustrated in Figure 3, with detailed functional forms and hyperparameter priors provided in Appendix B.

⁴We correct a minor error in their derivation. Our derivation can be found in Appendix A.3

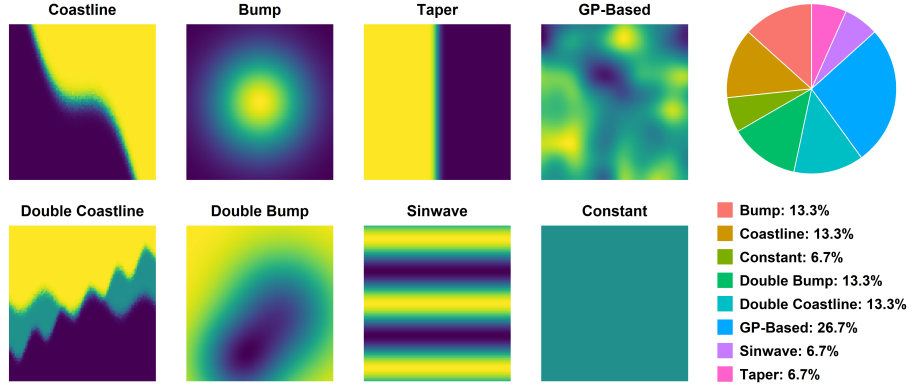


Figure 3: Spatial patterns (left) and their frequency (right).

Once a pattern $p^{(i)}$ and its hyperparameters $\Omega^{(i)}$ have been chosen, we then sample values from the prior distribution of the specific parameter (κ^2 , ρ , or θ) that we are constructing a field for. Each pattern (except ‘‘Constant’’) requires sampling two values which dictate the maximum and minimum value across the resulting parameter field. We set uniform priors on the anisotropy parameters $\rho \sim \mathcal{U}(1, 7)$ and $\theta \sim \mathcal{U}(-\frac{\pi}{2}, \frac{\pi}{2})$, and set a mixed prior of $\kappa^2 \sim 0.6 \log \mathcal{U}(10^{-4}, 2) + 0.4 \mathcal{U}(10^{-4}, 2)$ for the correlation range. These choices ensure we capture a broad range of spatial relationships, ranging from isotropy ($\rho = 1$) to very elongated ellipses ($\rho \gg 1$) in any direction.

We follow this process each time to create a parameter field for $\kappa^2(\mathbf{s})$, $\rho(\mathbf{s})$, and $\theta(\mathbf{s})$, and then encode all parameters into the SAR matrix B , as described in Section 2. Drawing white noise $\mathbf{e} \sim \mathcal{N}(0, I)$ and solving $B\mathbf{y} = \mathbf{e}$ yields a random field \mathbf{y} with the desired spatial covariance structure. Repeating this for M independent draws produces a small ensemble $Y = \{\mathbf{y}^{(m)}\}_{m=1}^M$ of different synthetic fields with identical covariance structures.

CNN data. For the local estimation setting, we assume local stationarity: within a small spatial window, all grid cells are governed by the same parameters. This makes data generation for the CNN comparatively straightforward. Rather than constructing parameter fields, we independently sample a single value for each of (κ^2, ρ, θ) from the prior distributions defined above. These parameters are then encoded into a SAR matrix B , resulting in stationary synthetic fields. We generate smaller fields than for the I2I networks, with each sample consisting of M replicates $\mathcal{Y} \in \mathbb{R}^{M \times h \times w}$, where $h \ll H$ and $w \ll W$. The associated ground truth is a parameter vector $\phi = [\kappa^2, \rho, \theta]^T \in \mathbb{R}^3$. Thus, our input-output pairs are (\mathcal{Y}, ϕ) .

4 Parameter estimation networks

We adapt three I2I networks for parameter estimation: a fully convolutional U-Net [59], a modified ViT [16], and a hybrid network inspired by the TransUNet [9] architecture. In each case we adhere closely to the original design, making only minimal or task-specific changes. A range of CNNs representative of the local estimation literature serve as our baselines.

UNet. We use a standard U-Net [59] with a symmetric encoder-bottleneck-decoder structure and skip connections that propagate spatial information across resolutions. Our implementation replaces ReLU with GELU activations [25], employs group normalization [83], and omits dropout [71]. The number of channels in the bottleneck matches the transformer embedding dimension used in the transformer-based I2I networks.

ViT. The original ViT was designed for image classification [16], so we remove classification-specific components such as the class token and final MLP head, and use a learnable linear layer to project the transformer output back to the original image resolution. The original 1D positional embeddings are replaced with a range of 2D alternatives; see Section 5.

STUN. Our hybrid architecture, a spatial TransUNet (STUN), is based on the network in [9], which was originally designed for image segmentation. It blends the two I2I networks discussed above, originally combining a pretrained convolutional encoder with a vision transformer and a shallow decoder. We retain the overall structure, but replace the encoder and decoder with the symmetric U-Net components used in our fully convolutional network.

CNN. Our local estimators follow the standard design of convolutional layers and a max pooling layer followed by an MLP. We use three networks with varying receptive window sizes that are representative of the local estimation literature [1, 35, 19, 64, 82]. The key difference is our networks have more parameters (1-2.5M), as compared to typical local estimators (50-700k).

4.1 Implementation and training details

All networks are trained with a batch size of $b = 64$ and varying numbers of replicate input fields $M \in \{1, 5, 15, 30\}$. Unless otherwise noted, all reported network sizes and metrics correspond to $M = 30$ replicates. For the I2I networks, each training example consists of M input fields of shape $[b, M, H, W] = [64, M, 192, 288]$, with corresponding output parameter fields $[64, 3, 192, 288]$. For the local CNN estimators, we vary the receptive field $h = w = \{9, 17, 25\}$, with inputs of shape $[64, M, h, w]$ and scalar outputs $[64, 3]$. We append the window size to the name of the CNN, thus $h = w = 25$ is denoted CNN25. To encourage permutation invariance, we randomly shuffle the replicates across the channel dimension each training step, imposing a soft constraint. This avoids sacrificing network expressiveness, which is a concern when imposing a hard constraint via an aggregation step [86]. We take care to preserve key elements of the statistical structure of the images, which are not compatible with data augmentation techniques such as image rotation, which does not preserve the angle of anisotropy θ . Thus, we limit augmentation to spatial translation and random field negation. We generate datasets consisting of 8000 (I2I) and 80000 (CNN) samples with 30 replicates, and employ a 90/8/2 (train/validation/test) split, resulting in a test set of 160 samples for the I2I dataset, which both local and global methods are evaluated on in the following section. More details on implementation, storage, and software can be found in Appendix C.

5 Simulated data experiments

We generate a test set of 160 samples following the procedure in Section 3. Each sample is a small ensemble $Y \in \mathbb{R}^{M \times 192 \times 288}$ of M replicates and an associated parameter image $\Phi \in \mathbb{R}^{3 \times 192 \times 288}$. For the I2I networks (UNet, ViT, STUN) we simply forward-propagate Y to obtain $\hat{\Phi}_{\text{I2I}}$. For the local CNN baselines, we employ a pixel-by-pixel approach: we translate the CNN window across the field with a stride of 1, assigning the prediction to the central pixel of the window to build $\hat{\Phi}_{\text{CNN}}$. We use reflection padding—improving upon prior works which use zero padding—thus reducing edge-artifacts. Figure 4 contrasts an example Φ with estimates from the best performing global (STUN) and local (CNN25) networks. MLE is not attempted; local likelihood evaluation for one field would require hundreds of hours, exceeding the total runtime of our approach by orders of magnitude [82].

Positional embeddings. The spatial nature of our problem leads us to study the effects of positional embeddings. We evaluate four embeddings for the transformer: none, 2-D sinusoidal [50], learned 2-D [16], and rotary (RoPE) [74]. RoPE yields the best performance across the majority of metrics for both ViT and STUN, and is adopted henceforth (see Appendix Table 2).

Number of replicates. We observe the effect on parameter estimation performance with varying numbers of replicates $M = \{1, 5, 15, 30\}$. Table 1 compares results for the extremes of this range. We find that I2I networks are more resilient to a low number of replicates, with STUN and UNet showing almost no difference in prediction RMSE. Full results are in Appendix Tables 3, 4.

Our experiments highlight three consistent trends. (i) Global I2I networks pose a significant improvement over local CNNs: STUN and UNet often display 4-5x lower RMSE and are almost unaffected by shrinking the ensemble size, whereas CNNs are noticeably sensitive. (ii) Adding attention helps only marginally in this setting, and attention on its own lags behind approaches that include multiscale convolutions. STUN edges out UNet but at 4x the parameter count. ViT lags behind the other I2I networks, perhaps as it requires more training data [16]. (iii) Global I2I networks take longer to train due

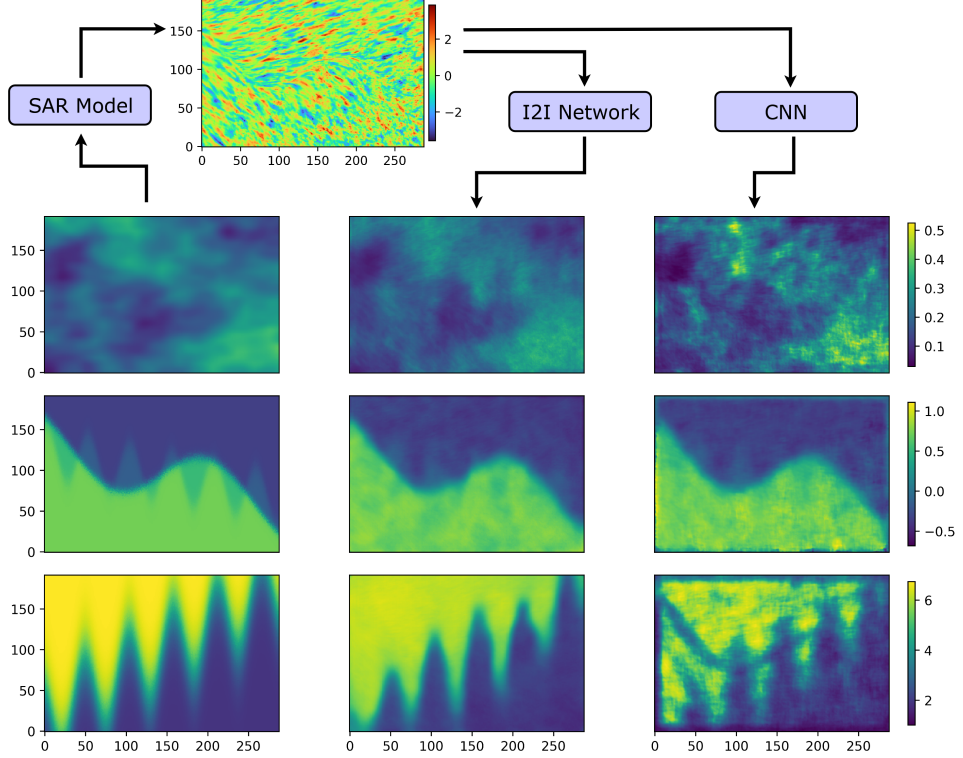


Figure 4: True parameters Φ (left) are encoded into the LatticeKrig SAR model to simulate a testing sample Y , of which one replicate $y^{(0)}$ is displayed. Y is used as an input to STUN and a sliding window, local estimation strategy using CNN25, resulting in $\hat{\Phi}_{\text{STUN}}$ (middle), and $\hat{\Phi}_{\text{CNN25}}$ (right).

Table 1: Root mean square error (RMSE) for parameter estimation on simulated test set using 1 and 30 replicates (reps). “Size” is the net parameter count (in millions). “Train” is the wall-clock time for training until early stopping, and “Eval” is the average time (out of 5) to process the 160 sample test dataset. Arrows indicate desirable direction, and bold values indicate best performance.

Net	30 rep RMSE ↓			1 rep RMSE ↓			Size (M) ↓	Train (min) ↓	Eval (sec) ↓
	κ^2	ρ	θ	κ^2	ρ	θ			
CNN9	0.963	0.937	0.316	1.01	1.39	0.535	1.3	8	71.3
CNN17	0.765	0.994	0.293	0.766	1.27	0.443	1.9	19	163.0
CNN25	0.743	1.03	0.272	0.806	1.28	0.418	2.6	35	341.6
ViT	0.374	0.625	0.204	0.471	0.771	0.237	92	161	0.30
UNet	0.201	0.308	0.087	0.195	0.354	0.111	25	144	0.33
STUN	0.189	0.302	0.091	0.189	0.351	0.097	105	178	0.38

to a higher parameter count, yet are *amortized* at inference time. In order to achieve the results of a single forward pass through an I2I network, the local estimators must perform $H \times W = 55,296$ forward passes. Consequently, I2I networks perform inference 100–1000 times faster than local estimators.

6 Climate application

We evaluate our framework on a 30-member ensemble of surface temperature sensitivity fields from the Community Earth System Model Large Ensemble (CESM1 LENS) project [29]. Each field is defined on a grid of approximately one degree resolution (192×288), and represents the local change in temperature given an increase of 1°C in global temperature. Due to the chaotic nature of the ocean-atmosphere system, we can treat these 30 estimates of temperature sensitivity as

independent replicates from the “true” climate sensitivity of CESM1. The data is preprocessed into standardized temperature sensitivity anomalies where each pixel has zero mean and unit variance. We then perform parameter estimation with the best global (STUN) and local (CNN25) estimation networks. Regardless of the estimation method used, our SAR model simulates 1000 fields in less than 10 seconds on a single laptop CPU, a stark contrast to the tens of millions of core hours required to generate the original 30-member ensemble.

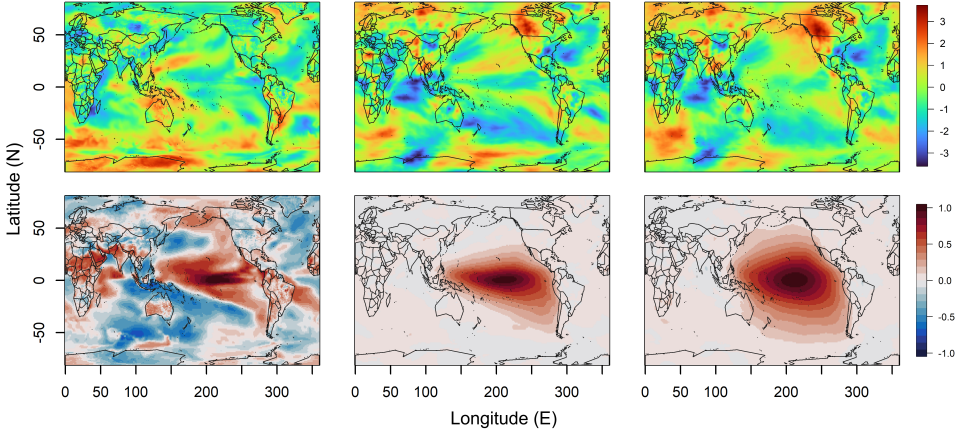


Figure 5: **Top:** Standardized temperature fields drawn from the CESM1 LENS ensemble (**left**), the STUN-based emulator (**middle**), and the CNN25-based emulator (**right**). **Bottom:** Correlations with a chosen location in the Niño 3.4 region at $(212^{\circ}\text{E}, 1^{\circ}\text{N})$ for the same three ensembles. The STUN-based emulator better preserves spatial relationships, including the zonal correlation structure along the equator and the meridional oceanic correlation range.

We use the STUN-based and CNN25-based emulators to generate 1000 fields each, and evaluate how well these synthetic ensembles preserve the spatial relationships present in the CESM outputs. Absolute prediction error is not meaningful here as the “truth” is itself a Monte-Carlo sample of internal climate variability. Thus, we compare the second-order structure through a covariance analysis. Rather than computing the entire $55,296 \times 55,296$ correlation matrices of the true and simulated fields, we compare a representative sample of 50 rows. First, we randomly select 50 anchor locations. For each of the three ensembles, we then calculate each anchor’s Pearson correlation with every other location. The average RMSE between these 50 true rows and their simulated counterparts is 0.229 for the STUN-based and 0.243 for CNN25-based emulation. A paired t-test demonstrates the strong statistical significance ($p_{\text{value}} = 1.1 \times 10^{-6} < 0.01 = \alpha$) of this difference (full results in Appendix E). Visualizing the empirical correlations with a chosen point in the Niño3.4 region—a region of the tropical pacific most correlated with the El Niño-Southern Oscillation phenomenon [3]—provides a qualitative comparison of the two methods (Figure 5). The STUN-based emulator better preserves the expected zonal east-west correlation structure along the equator with a more realistic correlation range. The CNN-based emulator systematically over-smooths and inflates the oceanic correlation range, particularly in the meridional north-south direction. The original ensemble correlation field is noisier due to the CESM1 LENS ensemble only containing 30 members. In sum, the STUN method outperforms the CNN method both quantitatively and qualitatively in representing the underlying correlation structure of climate sensitivity fields.

7 Related works

Neural parameter estimation. In situations where the likelihood function is intractable, but simulation from the model is feasible, neural networks have emerged as a powerful alternative [39, 87] to MLE [82]. Neural parameter estimation combines ideas from simulation-based inference [12, 69] and learning to optimize (L2O) [11, 84] by training networks to identify maxima of the Bayes risk [64]. The training cost is then amortized by repeated use. Until now, these approaches have been limited to local estimation [1, 35, 64, 55, 19, 54], typically using multi-layer perceptrons (MLPs) and CNNs. This line of research is the main inspiration for this work, which advances the field with simultaneous, non-stationary parameter inference and the use of I2I networks. Our network

choices [59, 16, 9] establish a baseline, and there exist many additional architectures for future work to explore [5, 56, 31, 78, 2].

Climate model emulation. While climate model emulation is not the sole application of our method, it provides an illustrative example and grounds our discussion of related, non-stationary emulation literature. Physics-based climate models require tens to hundreds of millions of core hours, necessitating data-driven emulation [27, 17]. Despite recent advances in deterministic [52, 34, 46, 4, 44, 30, 10] and ensemble-based probabilistic [32, 53, 36, 67] weather forecasting, comparatively fewer methods focus explicitly on long-term climate projections [33, 27, 17]. Our approach draws ideas from statistical methods, which explicitly link parameter estimation with emulation [6, 70, 48, 82, 7], and machine learning (ML) methods, both deterministic [45, 80, 8] and probabilistic [62, 61] which emulate directly from initial forcings or prior timesteps. Specifically, we combine the straightforward uncertainty quantification and interpretable parameters from the statistical model with a deterministic ML approach for efficient parameter estimation. Purely ML-based climate emulators typically require an extensive corpus of training data [79, 85] and can exhibit limited generalization capabilities beyond their training distributions [26]. We sidestep this by generating synthetic training data that mimics non-stationarity in geophysical settings. Our framework does not serve as a replacement for ESMs, but rather a complementary method for augmenting ensemble sizes, and reducing the number of “ground truth” ESM runs that must be computed.

8 Limitations and extensions

The limitations of this work fall into two categories: those of the I2I networks, and those of the statistical model.

Estimation networks. Our I2I networks assume complete, regularly gridded data and are trained on fixed input dimensions. While the architectures can process variable resolutions, generalization across sizes remains untested. Replicate count is also fixed at training time, with only a soft constraint to enforce permutation invariance. A hard constraint via aggregation [86] could resolve this, although the potential to limit network expressiveness must be explored. The performance of the transformer-based networks would likely benefit from efficient training regimes [76] and a larger dataset. Future work could extend the data generation pipeline to accommodate variable dataset dimensions and explore scalable attention mechanisms for larger spatial domains [5].

Statistical model. We adopt a Gaussian process framework via SAR approximation, which enforces monotonic decay of the covariance and cannot capture global teleconnections or nonlinear dynamics such as eddies. Our current formulation omits explicit modeling of an additional white noise process, and could benefit from increased smoothing in areas with long-range correlation structures. Extensions to this work could explore multi-resolution structures [28, 63, 47], estimate a spatially varying noise term, and approximate nonlocal dependence patterns that arise in physical systems.

While our framework enables efficient simulation of plausible ensembles, it ultimately inherits the assumptions and constraints of the underlying statistical model. Applications beyond climate model emulation—such as epidemiology, hydrology, or materials science—are feasible, although they may require tailoring the data generation strategy and retraining.

9 Conclusion

We introduce LatticeVision, a global, image-to-image (I2I) framework for the estimation and emulation of non-stationary spatial processes. By representing both the spatial fields and parameters as images, we employ vision networks to simultaneously estimate all parameters in a single forward pass. We develop a novel, non-stationary data generation pipeline for training such networks without relying on a large, existing corpus of application-specific data. As compared to local approaches, I2I networks demonstrate improvements in accuracy, robustness with few replicates, estimation speed, and ability to capture long-range, anisotropic correlations. We pair these estimators with the LatticeKrig SAR model, enabling fast simulation of large ensembles for non-stationary spatial data.

10 Acknowledgements

We would like to thank Ryan Peterson, Ryker Fish, Sweta Rai, Brandon Knutson, and Samy Wu Fung for their insights and helpful discussions. This material is based upon work supported by the National Science Foundation Graduate Research Fellowship Program under Grant No. DGE-2137099. Any opinions, findings, and conclusions or recommendations expressed in this material are those of the authors and do not necessarily reflect the views of the National Science Foundation. Nathan Lenssen is partially funded through NCAR which is sponsored by the National Science Foundation under Cooperative Agreement 1852977.

References

- [1] Divya Banesh et al. “Fast Gaussian process estimation for large-scale in situ inference using convolutional neural networks”. In: *2021 IEEE International Conference on Big Data (Big Data)*. IEEE. 2021, pp. 3731–3739.
- [2] Yujia Bao, Srinivasan Sivanandan, and Theofanis Karaletsos. “Channel vision transformers: An image is worth 1 x 16 x 16 words”. In: *arXiv preprint arXiv:2309.16108* (2023).
- [3] Anthony G Barnston, Muthuvel Chelliah, and Stanley B Goldenberg. “Documentation of a highly ENSO-related SST region in the equatorial Pacific: Research note”. In: *Atmosphere-ocean* 35.3 (1997), pp. 367–383.
- [4] Kaifeng Bi et al. “Accurate medium-range global weather forecasting with 3D neural networks”. In: *Nature* 619.7970 (2023), pp. 533–538.
- [5] Hu Cao et al. “Swin-unet: Unet-like pure transformer for medical image segmentation”. In: *European conference on computer vision*. Springer. 2022, pp. 205–218.
- [6] Stefano Castruccio et al. “Statistical emulation of climate model projections based on precomputed GCM runs”. In: *Journal of Climate* 27.5 (2014), pp. 1829–1844.
- [7] Anirban Chakraborty and Matthias Katzfuss. “Learning non-Gaussian spatial distributions via Bayesian transport maps with parametric shrinkage”. In: *Journal of Agricultural, Biological and Environmental Statistics* (2025), pp. 1–19.
- [8] William E Chapman et al. “CAMulator: Fast Emulation of the Community Atmosphere Model”. In: *arXiv preprint arXiv:2504.06007* (2025).
- [9] Jieneng Chen et al. “Transunet: Transformers make strong encoders for medical image segmentation”. In: *arXiv preprint arXiv:2102.04306* (2021).
- [10] Kang Chen et al. “Fengwu: Pushing the skillful global medium-range weather forecast beyond 10 days lead”. In: *arXiv preprint arXiv:2304.02948* (2023).
- [11] Tianlong Chen et al. “Learning to optimize: A primer and a benchmark”. In: *Journal of Machine Learning Research* 23.189 (2022), pp. 1–59.
- [12] Kyle Cranmer, Johann Brehmer, and Gilles Louppe. “The frontier of simulation-based inference”. In: *Proceedings of the National Academy of Sciences* 117.48 (2020), pp. 30055–30062.
- [13] Noel Cressie. *Statistics for spatial data*. John Wiley & Sons, 2015.
- [14] Noel Cressie and Gardar Johannesson. “Fixed rank kriging for very large spatial data sets”. In: *Journal of the Royal Statistical Society Series B: Statistical Methodology* 70.1 (2008), pp. 209–226.
- [15] Clara Deser et al. “Insights from Earth system model initial-condition large ensembles and future prospects”. In: *Nature Climate Change* 10.4 (2020), pp. 277–286.
- [16] Alexey Dosovitskiy. “An image is worth 16x16 words: Transformers for image recognition at scale”. In: *arXiv preprint arXiv:2010.11929* (2020).
- [17] Veronika Eyring et al. “Pushing the frontiers in climate modelling and analysis with machine learning”. In: *Nature Climate Change* 14.9 (2024), pp. 916–928.
- [18] Montserrat Fuentes. “Spectral methods for nonstationary spatial processes”. In: *Biometrika* 89.1 (2002), pp. 197–210.
- [19] Florian Gerber and Douglas Nychka. “Fast covariance parameter estimation of spatial Gaussian process models using neural networks”. In: *Stat* 10.1 (2021), e382.

[20] Subimal Ghosh and PP Mujumdar. “Climate change impact assessment: Uncertainty modeling with imprecise probability”. In: *Journal of Geophysical Research: Atmospheres* 114.D18 (2009).

[21] Rajarshi Guhaniyogi and Sudipto Banerjee. “Meta-kriging: Scalable Bayesian modeling and inference for massive spatial datasets”. In: *Technometrics* 60.4 (2018), pp. 430–444.

[22] Kai Han et al. “A survey on vision transformer”. In: *IEEE transactions on pattern analysis and machine intelligence* 45.1 (2022), pp. 87–110.

[23] Kathryn A Haskard, Brian R Cullis, and Arūnas P Verbyla. “Anisotropic Matérn correlation and spatial prediction using REML”. In: *Journal of agricultural, biological, and environmental statistics* 12 (2007), pp. 147–160.

[24] Matthew J Heaton et al. “A case study competition among methods for analyzing large spatial data”. In: *Journal of agricultural, biological and environmental Statistics* 24 (2019), pp. 398–425.

[25] Dan Hendrycks and Kevin Gimpel. “Gaussian error linear units (gelus)”. In: *arXiv preprint arXiv:1606.08415* (2016).

[26] Julia Kaltenborn et al. “Climateset: A large-scale climate model dataset for machine learning”. In: *Advances in Neural Information Processing Systems* 36 (2023), pp. 21757–21792.

[27] Karthik Kashinath et al. “Physics-informed machine learning: Case studies for weather and climate modelling”. In: *Philosophical Transactions of the Royal Society A* 379.2194 (2021), p. 20200093.

[28] Matthias Katzfuss. “A multi-resolution approximation for massive spatial datasets”. In: *Journal of the American Statistical Association* 112.517 (2017), pp. 201–214.

[29] Jennifer E Kay et al. “The Community Earth System Model (CESM) large ensemble project: A community resource for studying climate change in the presence of internal climate variability”. In: *Bulletin of the American Meteorological Society* 96.8 (2015), pp. 1333–1349.

[30] Ryan Keisler. “Forecasting global weather with graph neural networks”. In: *arXiv preprint arXiv:2202.07575* (2022).

[31] Soohyun Kim et al. “InstaFormer: Instance-aware image-to-image translation with transformer”. In: *Proceedings of the IEEE/CVF conference on computer vision and pattern recognition*. 2022, pp. 18321–18331.

[32] Dmitrii Kochkov et al. “Neural general circulation models for weather and climate”. In: *Nature* 632.8027 (2024), pp. 1060–1066.

[33] Ching-Yao Lai et al. “Machine learning for climate physics and simulations”. In: *Annual Review of Condensed Matter Physics* 16 (2024).

[34] Remi Lam et al. “Learning skillful medium-range global weather forecasting”. In: *Science* 382.6677 (2023), pp. 1416–1421.

[35] Amanda Lenzi et al. “Neural networks for parameter estimation in intractable models”. In: *Computational Statistics & Data Analysis* 185 (2023), p. 107762.

[36] Lizao Li et al. “Seeds: Emulation of weather forecast ensembles with diffusion models”. In: *arXiv preprint arXiv:2306.14066* (2023).

[37] Finn Lindgren, David Bolin, and Håvard Rue. “The SPDE approach for Gaussian and non-Gaussian fields: 10 years and still running”. In: *Spatial Statistics* 50 (2022), p. 100599.

[38] Finn Lindgren, Håvard Rue, and Johan Lindström. “An explicit link between Gaussian fields and Gaussian Markov random fields: The stochastic partial differential equation approach”. In: *Journal of the Royal Statistical Society Series B: Statistical Methodology* 73.4 (2011), pp. 423–498.

[39] Sulin Liu et al. “Task-agnostic amortized inference of Gaussian process hyperparameters”. In: *Advances in Neural Information Processing Systems* 33 (2020), pp. 21440–21452.

[40] Zhuang Liu et al. “A convnet for the 2020s”. In: *Proceedings of the IEEE/CVF conference on computer vision and pattern recognition*. 2022, pp. 11976–11986.

[41] Ilya Loshchilov and Frank Hutter. “Decoupled weight decay regularization”. In: *arXiv preprint arXiv:1711.05101* (2017).

[42] Bertil Matérn. *Spatial variation*. Vol. 36. Springer Science & Business Media, 2013.

[43] Sebastian Milinski, Nicola Maher, and Dirk Olonscheck. “How large does a large ensemble need to be?” In: *Earth System Dynamics* 11.4 (2020), pp. 885–901.

[44] Juan Nathaniel et al. “Chaosbench: A multi-channel, physics-based benchmark for subseasonal-to-seasonal climate prediction”. In: *arXiv preprint arXiv:2402.00712* (2024).

[45] Tung Nguyen et al. “ClimaX: A foundation model for weather and climate”. In: *arXiv preprint arXiv:2301.10343* (2023).

[46] Tung Nguyen et al. “Scaling transformer neural networks for skillful and reliable medium-range weather forecasting”. In: *Advances in Neural Information Processing Systems* 37 (2024), pp. 68740–68771.

[47] Douglas Nychka et al. “A multiresolution Gaussian process model for the analysis of large spatial datasets”. In: *Journal of Computational and Graphical Statistics* 24.2 (2015), pp. 579–599.

[48] Douglas Nychka et al. “Modeling and emulation of nonstationary Gaussian fields”. In: *Spatial statistics* 28 (2018), pp. 21–38.

[49] Douglas Nychka et al. *Package ‘LatticeKrig’*. 2019.

[50] Niki Parmar et al. “Image transformer”. In: *International conference on machine learning*. PMLR. 2018, pp. 4055–4064.

[51] A Paszke. “Pytorch: An imperative style, high-performance deep learning library”. In: *arXiv preprint arXiv:1912.01703* (2019).

[52] Jaideep Pathak et al. “Fourcastnet: A global data-driven high-resolution weather model using adaptive Fourier neural operators”. In: *arXiv preprint arXiv:2202.11214* (2022).

[53] Ilan Price et al. “Gencast: Diffusion-based ensemble forecasting for medium-range weather”. In: *arXiv preprint arXiv:2312.15796* (2023).

[54] Sweta Rai, Douglas W Nychka, and Soutir Bandyopadhyay. “Modeling Spatial Extremes using Non-Gaussian Spatial Autoregressive Models via Convolutional Neural Networks”. In: *arXiv preprint arXiv:2505.03034* (2025).

[55] Sweta Rai et al. “Fast parameter estimation of generalized extreme value distribution using neural networks”. In: *Environmetrics* 35.3 (2024), e2845.

[56] Yongming Rao et al. “Hornet: Efficient high-order spatial interactions with recursive gated convolutions”. In: *Advances in Neural Information Processing Systems* 35 (2022), pp. 10353–10366.

[57] Keith B Rodgers et al. “Ubiquity of human-induced changes in climate variability”. In: *Earth System Dynamics* 12.4 (2021), pp. 1393–1411.

[58] Robin Rombach et al. “High-resolution image synthesis with latent diffusion models”. In: *Proceedings of the IEEE/CVF conference on computer vision and pattern recognition*. 2022, pp. 10684–10695.

[59] Olaf Ronneberger, Philipp Fischer, and Thomas Brox. “U-net: Convolutional networks for biomedical image segmentation”. In: *Medical image computing and computer-assisted intervention–MICCAI 2015: 18th international conference, Munich, Germany, October 5–9, 2015, proceedings, part III* 18. Springer. 2015, pp. 234–241.

[60] Cynthia Rosenzweig et al. “Assessing agricultural risks of climate change in the 21st century in a global gridded crop model intercomparison”. In: *Proceedings of the national academy of sciences* 111.9 (2014), pp. 3268–3273.

[61] Salva Rühling Cachay et al. “Dyffusion: A dynamics-informed diffusion model for spatiotemporal forecasting”. In: *Advances in neural information processing systems* 36 (2023), pp. 45259–45287.

[62] Salva Rühling Cachay et al. “Probabilistic Emulation of a Global Climate Model with Spherical DYffusion”. In: *Advances in Neural Information Processing Systems* 37 (2024), pp. 127610–127644.

[63] Matthew Sainsbury-Dale, Andrew Zammit-Mangion, and Noel Cressie. “Modelling Big, Heterogeneous, Non-Gaussian Spatial and Spatio-Temporal Data using FRK”. In: *arXiv preprint arXiv:2110.02507* (2021).

[64] Matthew Sainsbury-Dale, Andrew Zammit-Mangion, and Raphaël Huser. “Likelihood-free parameter estimation with neural Bayes estimators”. In: *The American Statistician* 78.1 (2024), pp. 1–14.

[65] Matthew Sainsbury-Dale et al. “Neural Bayes estimators for irregular spatial data using graph neural networks”. In: *Journal of Computational and Graphical Statistics* just-accepted (2024), pp. 1–28.

[66] Kevin Schwarzwald and Nathan Lenssen. “The importance of internal climate variability in climate impact projections”. In: *Proceedings of the National Academy of Sciences* 119.42 (2022), e2208095119.

[67] Jimeng Shi et al. “Codicast: Conditional diffusion model for weather prediction with uncertainty quantification”. In: *arXiv preprint arXiv:2409.05975* (2024).

[68] Antony Sikorski, Daniel McKenzie, and Douglas Nychka. “Normalizing Basis Functions: Approximate Stationary Models for Large Spatial Data”. In: *Stat* 13.4 (2024), e70015.

[69] Scott A Sisson, Yanan Fan, and Mark Beaumont. *Handbook of approximate Bayesian computation*. CRC press, 2018.

[70] Yan Song, Zubair Khalid, and Marc G Genton. “Efficient stochastic generators with spherical harmonic transformation for high-resolution global climate simulations from CESM2-LENS2”. In: *Journal of the American Statistical Association* 119.548 (2024), pp. 2493–2507.

[71] Nitish Srivastava et al. “Dropout: A simple way to prevent neural networks from overfitting”. In: *The journal of machine learning research* 15.1 (2014), pp. 1929–1958.

[72] Michael L Stein. “A modeling approach for large spatial datasets”. In: *Journal of the Korean Statistical Society* 37 (2008), pp. 3–10.

[73] Michael L Stein. *Interpolation of spatial data: Some theory for kriging*. Springer Science & Business Media, 1999.

[74] Jianlin Su et al. “Roformer: Enhanced transformer with rotary position embedding”. In: *Neurocomputing* 568 (2024), p. 127063.

[75] Ying Sun, Bo Li, and Marc Genton. “Geostatistics for Large Datasets”. In: (Jan. 2012). DOI: 10.1007/978-3-642-17086-7_3.

[76] Hugo Touvron et al. “Training data-efficient image transformers & distillation through attention”. In: *International conference on machine learning*. PMLR. 2021, pp. 10347–10357.

[77] Thorsten Wagener, Robert Reinecke, and Francesca Pianosi. “On the evaluation of climate change impact models”. In: *Wiley Interdisciplinary Reviews: Climate Change* 13.3 (2022), e772.

[78] Wenhui Wang et al. “Pyramid vision transformer: A versatile backbone for dense prediction without convolutions”. In: *Proceedings of the IEEE/CVF international conference on computer vision*. 2021, pp. 568–578.

[79] Duncan Watson-Parris et al. “ClimateBench v1.0: A benchmark for data-driven climate projections”. In: *Journal of Advances in Modeling Earth Systems* 14.10 (2022), e2021MS002954.

[80] Oliver Watt-Meyer et al. “ACE: A fast, skillful learned global atmospheric model for climate prediction”. In: *arXiv preprint arXiv:2310.02074* (2023).

[81] Peter Whittle. “On stationary processes in the plane”. In: *Biometrika* (1954), pp. 434–449.

[82] Ashton Wiens, Douglas Nychka, and William Kleiber. “Modeling spatial data using local likelihood estimation and a Matérn to spatial autoregressive translation”. In: *Environmetrics* 31.6 (2020), e2652.

[83] Yuxin Wu and Kaiming He. “Group normalization”. In: *Proceedings of the European conference on computer vision (ECCV)*. 2018, pp. 3–19.

[84] Wotao Yin, Daniel McKenzie, and Samy Wu Fung. “Learning to Optimize: Where Deep Learning Meets Optimization and Inverse Problems”. In: *SIAM News* (2022).

[85] Sungduk Yu et al. “ClimSim: A large multi-scale dataset for hybrid physics-ML climate emulation”. In: *Advances in Neural Information Processing Systems* 36 (2023), pp. 22070–22084.

[86] Manzil Zaheer et al. “Deep sets”. In: *Advances in neural information processing systems* 30 (2017).

[87] Andrew Zammit-Mangion, Matthew Sainsbury-Dale, and Raphaël Huser. “Neural methods for amortized inference”. In: *Annual Review of Statistics and Its Application* 12 (2024).

A Anisotropic SAR derivation

A.1 The Matérn covariance

Under the Matérn family, Equation (1) takes the form:

$$k(\mathbf{s}, \mathbf{s}') = \sigma^2 \frac{2^{1-\nu}}{\Gamma(\nu)} (\kappa_m \|\mathbf{s} - \mathbf{s}'\|)^\nu \mathcal{K}_\nu(\kappa_m \|\mathbf{s} - \mathbf{s}'\|), \quad (7)$$

where $\Gamma(\cdot)$ is the gamma function, and $\mathcal{K}_\nu(\cdot)$ is the modified Bessel function of the second kind.

A.2 Isotropic SAR

In two dimensions ($\mathbf{s} \in \mathbb{R}^2$), with $\nu = 1$, Equation (2) can be written as

$$(\kappa^2 - \Delta) f(\mathbf{s}) = \mathcal{W}(\mathbf{s}), \quad (8)$$

where $\Delta = \partial^2 / \partial x^2 + \partial^2 / \partial y^2$ is the Laplacian operator. Let the domain be covered by a square lattice with unit spacing. We denote $f_{i,j} \equiv f(\mathbf{s}_{i,j})$ at grid point $\mathbf{s}_{i,j} = (i, j)$, $i, j \in \{1, \dots, N\}$.

Using second order central-difference approximations for the Laplacian yields

$$-\Delta f_{i,j} \approx [4f_{i,j} - f_{i+1,j} - f_{i-1,j} - f_{i,j+1} - f_{i,j-1}]. \quad (9)$$

Substituting (9) into (8) results in

$$(\kappa^2 + 4) f_{i,j} - (f_{i+1,j} + f_{i-1,j} + f_{i,j+1} + f_{i,j-1}) = e_{i,j}, \quad (10)$$

where $e_{i,j}$ denotes the discrete version of the noise \mathcal{W} at location (i, j) . Equation (10) can be visualized in lattice notation using the following stencil:

$$\begin{array}{c|c|c} 0 & -1 & 0 \\ \hline -1 & \kappa^2 + 4 & -1 \\ \hline 0 & -1 & 0 \end{array} \quad (11)$$

illustrating the isotropic relationship between $f_{i,j}$ and its neighboring locations.

A.3 Anisotropic extension

To incorporate geometric anisotropy we replace the Laplacian in (8) by the *generalised* Laplacian $\nabla \cdot H \nabla$, where the positive-definite dispersion matrix $H \in \mathbb{R}^{2 \times 2}$ is

$$H = R^\top D^2 R, \quad R = \begin{bmatrix} \cos \theta & -\sin \theta \\ \sin \theta & \cos \theta \end{bmatrix}, \quad D = \begin{bmatrix} \sqrt{\rho} & 0 \\ 0 & 1/\sqrt{\rho} \end{bmatrix}. \quad (12)$$

Here, R is a rotation matrix parametrized by θ and D is a scaling matrix parametrized by ρ . For a constant H the anisotropic SPDE becomes

$$(\kappa^2 - \nabla \cdot H \nabla) f(\mathbf{s}) = \mathcal{W}(\mathbf{s}). \quad (13)$$

Using unit grid spacing and second-order central differences for the second-derivative terms,

$$\begin{aligned} \nabla \cdot H \nabla f_{i,j} &\approx H_{1,1}(f_{i+1,j} - 2f_{i,j} + f_{i-1,j}) + H_{2,2}(f_{i,j+1} - 2f_{i,j} + f_{i,j-1}) \\ &\quad + \frac{H_{1,2}}{2}[f_{i+1,j+1} - f_{i+1,j-1} - f_{i-1,j+1} + f_{i-1,j-1}]. \end{aligned} \quad (14)$$

Substituting the above expression into (13) results in

$$\begin{aligned} (\kappa^2 + 2H_{1,1} + 2H_{2,2})f_{i,j} - H_{1,1}(f_{i+1,j} + f_{i-1,j}) - H_{2,2}(f_{i,j+1} + f_{i,j-1}) \\ - \frac{H_{1,2}}{2}[f_{i+1,j+1} - f_{i+1,j-1} - f_{i-1,j+1} + f_{i-1,j-1}] = e_{i,j}. \end{aligned} \quad (15)$$

Equation (15) corresponds to the 3×3 stencil

$$\begin{array}{c|c|c} \frac{H_{1,2}}{2} & -H_{2,2} & -\frac{H_{1,2}}{2} \\ \hline -H_{1,1} & \kappa^2 + 2H_{1,1} + 2H_{2,2} & -H_{1,1} \\ \hline -\frac{H_{1,2}}{2} & -H_{2,2} & \frac{H_{1,2}}{2}. \end{array} \quad (16)$$

One incorporates non-stationarity by allowing H and κ^2 to vary in space, as shown in Equation (3).

B Non-stationary data generation details

The synthetic data generation pipeline for the I2I networks constructs parameter fields for $\kappa^2(\mathbf{s})$, $\rho(\mathbf{s})$, and $\theta(\mathbf{s})$. The parameters have the following prior distributions:

$$\kappa^2 \sim 0.6 \log \mathcal{U}(10^{-4}, 2) + 0.4 \mathcal{U}(10^{-4}, 2), \quad \rho \sim \mathcal{U}(1, 7), \quad \theta \sim \mathcal{U}(-\frac{\pi}{2}, \frac{\pi}{2}) \quad (17)$$

Each parameter field is independently created by selecting one of several spatial patterns, sampling associated hyperparameters from prior distributions, sampling parameter values for the maxima and minima of the field, and optionally stacking two patterns to increase complexity.

B.1 Spatial patterns

We design eight simple yet expressive spatial patterns $p(\mathbf{s})$, intended as caricatures of realistic geophysical variability. Here we express p as a generic value for κ^2 , ρ , or θ , our pattern's associated hyperparameters as Ω , and the x and y coordinates on the grid as $\mathbf{s}_x, \mathbf{s}_y$, respectively.

Constant: Uniform value across the domain.

- Functional Form: $p(\mathbf{s}) = p_{\text{constant}}$, where p_{constant} is a constant sampled from the prior.

Coastline: A sharp sigmoidal boundary, perturbed by sinusoidal "bumps".

- Functional Form:

$$p(\mathbf{s}) = p_{\text{low}} + \frac{p_{\text{high}} - p_{\text{low}}}{1 + \exp(-\gamma(\mathbf{s}_y - v(\mathbf{s}_x)))} \quad (18)$$

where $v(\mathbf{s}_x) = \alpha \mathbf{s}_x + \beta \sin(2\pi\omega \mathbf{s}_x) + \epsilon$, and $p_{\text{low}}, p_{\text{high}}$ are the lower and higher of the two independently sampled parameter values, dictating the maxima and minima of the pattern.

- Hyperparameters: $\Omega = (\alpha, \beta, \omega, \gamma)$, sampled from $\alpha \sim \mathcal{U}(-2, 2)$, $\beta \sim \mathcal{U}(0.1, 0.5)$, $\omega \sim \mathcal{U}(0.4, 3)$, and $\gamma \sim \mathcal{U}(3, 50)$.

Taper: Smooth transition between two values, based on a Gaussian CDF.

- Functional Form:

$$p(\mathbf{s}) = p_{\text{low}} \Psi(\mathbf{s}_x + \mathbf{s}_y; 0, \sigma) + p_{\text{high}} (1 - \Psi(\mathbf{s}_x + \mathbf{s}_y; 0, \sigma)) \quad (19)$$

where $\Psi(\cdot)$ denotes the standard normal cumulative distribution function (CDF).

- Hyperparameters: $\Omega = \sigma$, with $\sigma \sim \mathcal{U}(0.05, 1)$ controlling the sharpness of the transition.

Bump: A single, smooth, Gaussian peak.

- Functional Form:

$$p(\mathbf{s}) = p_{\text{constant}} + a_1 \exp\left(-\frac{\mathbf{s}_x^2 + \mathbf{s}_y^2}{\lambda_1}\right) \quad (20)$$

- Hyperparameters: $\Omega = (a_1, \lambda_1)$, with a_1 controlling the peak height and λ_1 controlling spread. In all cases $\lambda_1 \sim \mathcal{U}(0.2, 0.5)$, while a_1 varies. When making a $\kappa^2(\mathbf{s})$ field, $a_1 \sim \mathcal{U}(0.1, 0.5)$. For $\rho(\mathbf{s})$, $a_1 \sim \mathcal{U}(0.1, 1.5)$, and for $\theta(\mathbf{s})$, $a_1 \sim \mathcal{U}(0.1, \frac{\pi}{4})$.

Sinwave: Periodic variation along one spatial axis.

- Functional Form:

$$p(\mathbf{s}) = \begin{cases} p_{\text{constant}} + a \sin(\pi \omega \mathbf{s}_x), & (\text{horizontal}) \\ p_{\text{constant}} + a \cos(\pi \omega \mathbf{s}_y), & (\text{vertical}) \end{cases} \quad (21)$$

- Hyperparameters: $\Omega = (a, \omega, \text{orientation})$, where $\omega \sim \mathcal{U}(1.5, 5)$, orientation is sampled uniformly between horizontal and vertical, and a is constrained to stay within the bounds of the parameter one is constructing a field for.

Double Bump: Superposition of two independent Gaussian peaks located at different positions.

- Functional Form:

$$p(\mathbf{s}) = p_{\text{constant}} + a_1 \exp\left(-\frac{(\mathbf{s}_x - x_1)^2 + (\mathbf{s}_y - y_1)^2}{\lambda_1}\right) + a_2 \exp\left(-\frac{(\mathbf{s}_x - x_2)^2 + (\mathbf{s}_y - y_2)^2}{\lambda_2}\right) \quad (22)$$

- Hyperparameters: $\Omega = (a_1, a_2, \lambda_1, \lambda_2, x_1, y_1, x_2, y_2)$, with amplitudes, widths, and locations sampled as previously described in the above “Bump” configuration, and with centers $(x_1, y_1), (x_2, y_2)$ being randomly sampled locations within the spatial domain.

Double Coastline: Weighted superposition of two independent coastline patterns.

- Functional Form:

$$p(\mathbf{s}) = p_{\text{low}} + w_1 \text{Coastline}_1(\mathbf{s}) + w_2 \text{Coastline}_2(\mathbf{s}) \quad (23)$$

- Hyperparameters: $w_1 \sim \mathcal{U}(0.1, 0.9)$, $w_2 \sim \mathcal{U}(0.1, 1 - w_1)$, and each coastline has its own, independent $(\alpha, \beta, \omega, \gamma)$ parameters as described in the above “Coastline” configuration.

GP-Based: A smooth, stationary random field generated by a low-rank Gaussian process, either min-max rescaled or perturbed around a constant.

- Functional Form: A realization from a Gaussian process, constructed via low-rank basis function approximation:

$$p(\mathbf{s}) = \begin{cases} p_{\text{min}}, p_{\text{max}} \text{ rescaled field,} & (\text{min-max scaling}) \\ p_{\text{constant}} \times (1 \pm g(\mathbf{s})), & (\text{perturbation scaling}) \end{cases} \quad (24)$$

where $g(\mathbf{s})$ is a normalized low-rank GP realization, p_{constant} is a parameter value sampled from the prior distribution, and $p_{\text{min}}, p_{\text{max}}$ represent the minimum and maximum of a parameter’s prior distribution.

- Hyperparameters: $\Omega = (n_{\text{basis}}, \text{scaling choice})$, where $n_{\text{basis}} \sim \mathcal{U}\{6, 7, \dots, 32\}$ controls the number of basis functions used to generate the realization of the GP. The scaling choice is selected randomly: either
 - Min-max scaling: $p(\mathbf{s})$ is rescaled to span the full prior range, or
 - Perturbation scaling: $p(\mathbf{s})$ is a small multiplicative perturbation around p_{constant} , with perturbation magnitude drawn from a prior distribution.

B.2 Pattern stacking

To further increase the complexity of our fields, for each parameter field we randomly decide whether to linearly combine two independently generated patterns. Given fields $p_1(\mathbf{s})$ and $p_2(\mathbf{s})$, the final field is

$$p(\mathbf{s}) = w p_1(\mathbf{s}) + (1 - w) p_2(\mathbf{s}), \quad w \sim \mathcal{U}(0.1, 0.9) \quad (25)$$

Stacking introduces complex non-stationarity patterns beyond those generated by a single functional form, increasing the range of spatial patterns seen during training.

B.3 Resulting synthetic data

We repeat the process of selecting a pattern, sampling the pattern hyperparameters Ω , sampling the parameter values, and generating the resulting parameter field for $\kappa^2(\mathbf{s})$, $\rho(\mathbf{s})$, and $\theta(\mathbf{s})$. We then encode all parameter fields into the SAR matrix B , draw white noise $\mathbf{e} \sim \mathcal{N}(0, I)$ and solve $B \mathbf{y} = \mathbf{e}$. We repeat this for M independent draws of the white noise, resulting in a small ensemble $Y = \{\mathbf{y}^{(m)}\}_{m=1}^M$, with each field having the same covariance structure. We process these synthetic fields identically to the way we process the input ESM fields: we perform pixelwise standardization to ensure each pixel has a mean of 0 and a standard deviation of 1. The non-stationarity in our problem does not allow for more sophisticated normalization techniques [68], which either become computationally intractable, require a stationary structure, or are not applicable in this setting. An example spatial field and its associated parameter fields can be seen in Figure 6.

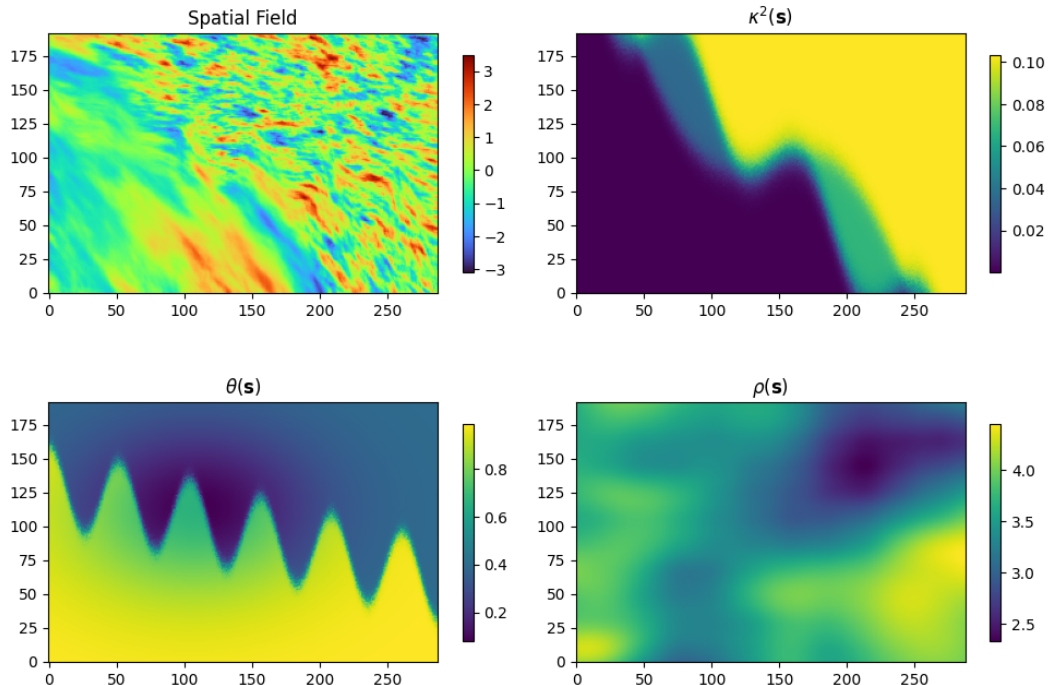


Figure 6: The first replicate in a training sample (**top-left**), and the accompanying parameter fields that were used to generate it (**remaining**). In this instance, a Double Coastline pattern was used for $\kappa^2(\mathbf{s})$, $\theta(\mathbf{s})$ is the result of stacked Coastline and Double Bump patterns, and $\rho(\mathbf{s})$ is created with a GP-Based pattern.

C Further implementation details

C.1 Data and storage

All data generation is done in the R programming language on a laptop with an Intel(R) Core(TM) i9-14900HX processor at 2.20 GHz, and 32GB of RAM. Fields are generated using the `LatticeKrig` package, and data is compressed and stored using the `hdf5` file format so it may be easily accessed in both Python and R. Storage proves to be more of a bottleneck as compared to data generation time: the I2I dataset (8,000 samples with 30 replicates) required 8 hours and occupies 108 GB, whereas the CNN dataset (80,000 samples with 30 replicates) is only 11 GB, and is generated in half an hour.

C.2 Training

All networks are implemented in PyTorch [51] and trained on a single NVIDIA RTX A6000 GPU. The networks are trained using the AdamW optimizer [41] for 200 epochs with a step-wise learning rate decay and early stopping after 10 epochs without validation improvement. We use mean squared error (MSE) loss, computed on normalized parameter values within the training loop. This avoids loss imbalance caused by parameter scale differences while requiring less pre or post-processing from the user.

D Further experiments with simulated data

In this section, Table 2 contains the results of experimenting with different positional embeddings for STUN and ViT. Tables 3 and 4 contain the results of experimenting across a different number of replicates $M = \{1, 5, 15, 30\}$ for all networks. In all tables, root mean squared error (RMSE), mean absolute error (MAE), and normalized RMSE (NRMSE) are calculated, along with the structural similarity index measure (SSIM) and peak signal to noise ratio (PSNR) in decibels (db) image comparison metrics.

Table 2: Results on simulated test data across different types of positional embeddings for both STUN and ViT. Best results for each architecture are in bold.

Net	Embedding	Param	Metrics				
			RMSE \downarrow	MAE \downarrow	SSIM (\uparrow to 1)	PSNR \uparrow	NRMSE \downarrow
ViT	None	κ^2	0.398	0.279	0.252	10.9	0.040
		ρ	0.711	0.525	0.277	6.41	0.118
		θ	0.249	0.124	0.251	13.6	0.083
	Sinusoidal	κ^2	0.393	0.274	0.275	10.8	0.040
		ρ	0.913	0.723	0.294	3.61	0.152
		θ	0.280	0.143	0.253	12.4	0.094
	Learned	κ^2	0.371	0.243	0.291	12.1	0.037
		ρ	0.920	0.715	0.288	3.30	0.153
		θ	0.351	0.193	0.235	9.83	0.117
	Rotary	κ^2	0.374	0.250	0.310	11.9	0.038
		ρ	0.625	0.465	0.337	7.01	0.104
		θ	0.204	0.103	0.328	15.1	0.068
STUN	None	κ^2	0.198	0.118	0.489	18.4	0.020
		ρ	0.311	0.213	0.548	14.2	0.052
		θ	0.096	0.046	0.604	21.7	0.032
	Sinusoidal	κ^2	0.190	0.113	0.483	18.7	0.019
		ρ	0.302	0.202	0.542	14.7	0.050
		θ	0.126	0.050	0.592	21.5	0.042
	Learned	κ^2	0.204	0.122	0.462	18.0	0.021
		ρ	0.309	0.217	0.522	13.9	0.052
		θ	0.090	0.045	0.595	21.8	0.030
	Rotary	κ^2	0.189	0.117	0.469	18.4	0.019
		ρ	0.302	0.212	0.531	14.3	0.050
		θ	0.091	0.044	0.594	21.9	0.030

E Further climate application results

We pass the standardized, 30-member ensemble of CESM1 LENS temperature sensitivity anomalies into each of our estimation networks: STUN, UNet, ViT, CNN25, CNN17, and CNN9. Using the predicted parameters, we generate 1,000 synthetic fields from each model. Generation is performed

Table 3: Results on simulated test data across varying replicates for image-to-image networks.

Net	Reps	Param	Metrics				
			RMSE \downarrow	MAE \downarrow	SSIM (\uparrow to 1)	PSNR \uparrow	NRMSE \downarrow
UNet	1	κ^2	0.195	0.125	0.447	17.6	0.020
		ρ	0.354	0.250	0.534	13.1	0.059
		θ	0.111	0.052	0.571	20.8	0.037
	5	κ^2	0.199	0.125	0.438	17.7	0.020
		ρ	0.319	0.223	0.527	13.8	0.053
		θ	0.115	0.053	0.546	20.5	0.038
	15	κ^2	0.180	0.110	0.503	18.9	0.018
		ρ	0.294	0.207	0.592	14.6	0.049
		θ	0.102	0.044	0.628	22.3	0.034
ViT	30	κ^2	0.201	0.124	0.447	17.9	0.020
		ρ	0.308	0.214	0.517	14.1	0.051
		θ	0.087	0.046	0.582	21.3	0.029
	1	κ^2	0.471	0.303	0.296	10.5	0.048
		ρ	0.771	0.588	0.328	5.36	0.129
		θ	0.237	0.113	0.323	14.3	0.079
	5	κ^2	0.377	0.243	0.326	12.3	0.038
		ρ	0.633	0.470	0.358	7.06	0.106
		θ	0.211	0.098	0.359	15.6	0.071
STUN	15	κ^2	0.354	0.229	0.324	12.6	0.036
		ρ	0.594	0.425	0.350	7.73	0.099
		θ	0.206	0.099	0.340	15.4	0.069
	30	κ^2	0.374	0.250	0.310	11.9	0.038
		ρ	0.625	0.465	0.337	7.01	0.104
		θ	0.204	0.103	0.328	15.1	0.068
	1	κ^2	0.189	0.124	0.470	17.7	0.019
		ρ	0.351	0.243	0.535	13.3	0.058
		θ	0.097	0.047	0.593	21.3	0.033
STUN	5	κ^2	0.180	0.109	0.502	18.8	0.018
		ρ	0.290	0.198	0.554	14.8	0.048
		θ	0.100	0.044	0.632	22.2	0.033
	15	κ^2	0.188	0.114	0.483	18.6	0.019
		ρ	0.303	0.209	0.551	14.4	0.051
		θ	0.102	0.047	0.589	21.6	0.034
	30	κ^2	0.189	0.117	0.469	18.4	0.019
		ρ	0.302	0.212	0.531	14.3	0.050
		θ	0.091	0.044	0.594	21.9	0.030

using the LatticeKrig R package [49], which accommodates cylindrical geometry and ensures the correct treatment of spatial distances under the Mercator projection.

To evaluate how well each synthetic ensemble preserves the spatial correlation structure, we randomly select 50 anchor locations and compute the corresponding 50 rows from each ensemble's empirical correlation matrix. These are then compared to the 50 rows from the original CESM1 ensemble's correlation matrix using root mean squared error (RMSE). We systematically pair each I2I network with a local CNN of comparable rank (e.g., STUN vs. CNN25, UNet vs. CNN17), and compare their RMSEs across the same anchor locations. As the anchor locations are fixed for all pairings, we conduct paired t-tests between matched RMSEs to compare performance.

Table 4: Results on simulated test data across varying replicates for local CNNs.

Net	Reps	Param	Metrics				
			RMSE \downarrow	MAE \downarrow	SSIM (\uparrow to 1)	PSNR \uparrow	NRMSE \downarrow
CNN9	1	κ^2	1.01	0.637	0.069	4.64	0.101
		ρ	1.39	1.09	0.02	-0.980	0.231
		θ	0.535	0.295	0.072	5.27	0.179
	5	κ^2	0.983	0.547	0.129	6.97	0.099
		ρ	1.03	0.760	0.052	2.02	0.172
		θ	0.346	0.149	0.217	10.5	0.116
	15	κ^2	0.949	0.512	0.160	7.81	0.096
		ρ	0.962	0.689	0.070	2.90	0.160
		θ	0.330	0.135	0.300	11.3	0.110
CNN17	30	κ^2	0.963	0.508	0.172	8.09	0.097
		ρ	0.937	0.660	0.085	3.28	0.156
		θ	0.316	0.121	0.347	11.7	0.106
	1	κ^2	0.766	0.480	0.086	6.45	0.077
		ρ	1.27	0.960	0.026	-0.062	0.212
		θ	0.443	0.200	0.147	7.60	0.148
	5	κ^2	0.828	0.443	0.169	8.52	0.084
		ρ	1.03	0.714	0.081	2.75	0.171
		θ	0.317	0.126	0.289	11.1	0.106
CNN25	15	κ^2	0.730	0.377	0.222	9.94	0.074
		ρ	0.939	0.614	0.123	4.00	0.157
		θ	0.266	0.097	0.411	12.0	0.089
	30	κ^2	0.764	0.397	0.212	9.63	0.077
		ρ	0.994	0.669	0.103	3.37	0.166
		θ	0.293	0.116	0.349	11.5	0.098
	1	κ^2	0.806	0.488	0.111	6.81	0.081
		ρ	1.28	0.949	0.036	0.164	0.214
		θ	0.418	0.179	0.215	8.21	0.140
CNN25	5	κ^2	0.767	0.409	0.166	9.0	0.077
		ρ	1.09	0.736	0.088	2.77	0.181
		θ	0.340	0.124	0.316	10.2	0.114
	15	κ^2	0.732	0.372	0.249	10.2	0.074
		ρ	1.03	0.669	0.150	3.71	0.172
		θ	0.279	0.107	0.445	11.5	0.093
	30	κ^2	0.743	0.378	0.256	10.1	0.075
		ρ	1.03	0.676	0.144	3.55	0.172
		θ	0.272	0.106	0.434	11.8	0.091

Our null hypothesis for each paired comparison is that the mean RMSE difference equals zero, $H_0: \mu_d = 0$, where $d = \text{RMSE}_{\text{I2I}} - \text{RMSE}_{\text{CNN}}$. The one-sided alternative, $H_1: \mu_d < 0$, states that the I2I emulator attains a lower RMSE than its CNN counterpart. All tests are conducted with a significance level $\alpha = 0.01$. Results are summarized in Table 5. For every comparison, the null hypothesis is rejected and the 99% confidence interval is entirely negative, demonstrating that each I2I network produces significantly more accurate correlation structure estimates than its corresponding local CNN.

Table 5: Paired t-test results comparing I2I-based emulators to corresponding CNN-based emulators on average RMSE across the same 50 anchor locations. CI denotes the 99% confidence interval of the paired differences.

Model pair	$\mu_{\text{I2I}} \downarrow$	$\mu_{\text{local}} \downarrow$	μ_d	99% CI	p_{value}
STUN vs. CNN25	0.229	0.243	-0.013	$(-\infty, -0.007]$	1.1×10^{-6}
UNet vs. CNN17	0.230	0.239	-0.008	$(-\infty, -0.004]$	3.4×10^{-5}
ViT vs. CNN9	0.228	0.244	-0.016	$(-\infty, -0.008]$	5.9×10^{-6}

Additionally, we provide analogous visual comparisons to Figure 5 for the UNet, CNN17, ViT, and CNN9 networks in Figure 7 and Figure 8, respectively. These figures highlight a few consistent trends: I2I emulators more accurately preserve the spatial correlation structure, particularly zonal features along the equator, while local CNNs tend to produce over-smoothed correlations with inflated meridional spread.

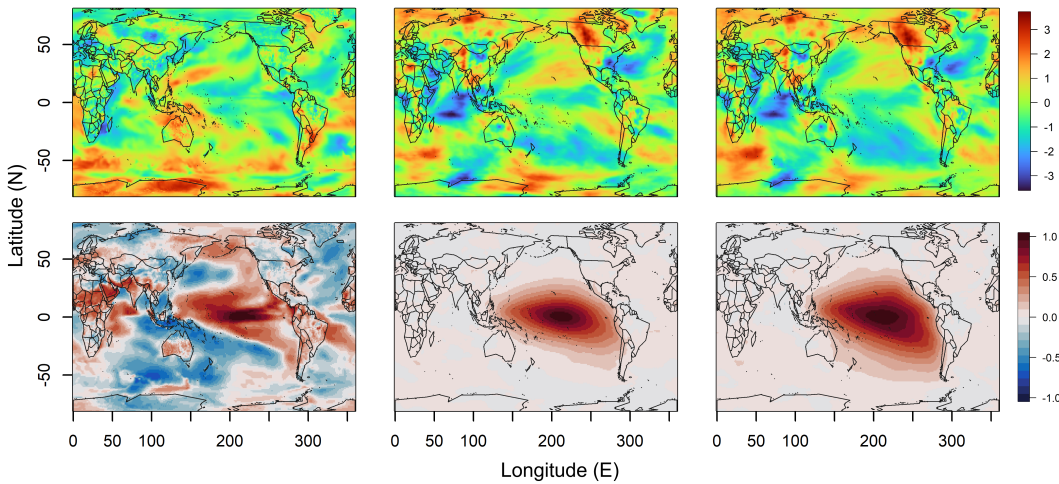


Figure 7: **Top:** Standardized temperature fields drawn from the CESM1-LENS ensemble (**left**), the UNet-based emulator (**middle**), and the CNN17-based emulator (**right**). **Bottom:** Correlations with a chosen location in the Niño 3.4 region at $(212^{\circ}\text{E}, 1^{\circ}\text{N})$ for the same three ensembles.

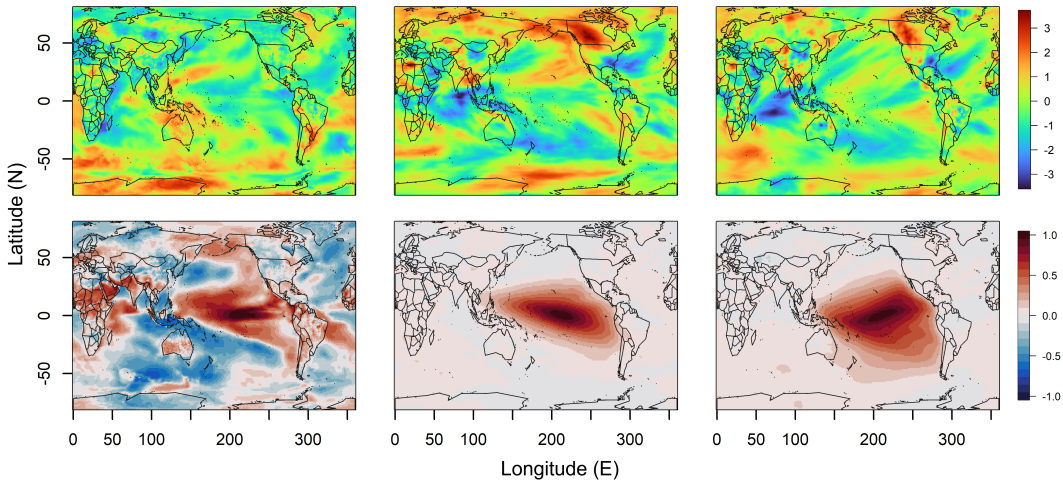


Figure 8: **Top:** Standardized temperature fields drawn from the CESM1-LENS ensemble (**left**), the ViT-based emulator (**middle**), and the CNN9-based emulator (**right**). **Bottom:** Correlations with a chosen location in the Niño 3.4 region at $(212^{\circ}\text{E}, 1^{\circ}\text{N})$ for the same three ensembles.